ACS EARTH AND SPACE CHEMISTRY

http://pubs.acs.org/journal/aesccq

Article

Competition between Abstraction and Addition Channels for the Reaction between the OH Radical and Vinyl Alcohol in the Interstellar Medium

Bernardo Ballotta,* Emilio Martínez-Núñez, Sergio Rampino, and Vincenzo Barone*

Cite This: *ACS Earth Space Chem.* 2023, 7, 1467−1477

Read Online

ACCESS | Metrics & More | Article Recommendations | Supporting Information

ABSTRACT: Vinyl alcohol (Vy) and hydroxyl radical (OH) are involved in several processes, which take place in environments characterized by very different physical−chemical conditions, ranging from the low pressures and temperatures typical of the interstellar medium (ISM) up to the high temperatures of interest for combustion processes. A gas-phase reaction mechanism involving Vy and OH has been proposed as a possible path for the formation of (*Z*)-1,2-ethenediol (Et), a molecule recently identified in the ISM. Et, the enolic form of glycolaldehyde, is considered a key precursor for the formation of sugars in both interstellar and prebiotic chemistry. We have therefore undertaken a detailed quantum chemical study of possible reaction channels starting from the interaction between the OH radical and both conformers of Vy (*syn* and *anti*). The formation of a prereactive complex always represents the first step of the reaction, which can then proceed through the attack to the C═C double bond (leading in turn to the formation of different dissociation products) or through hydrogen abstraction, which eventually produces a radical species and water. Then, a master equation approach based on ab initio transition state theory has been employed to calculate the reaction rate constants of different products for temperatures up to 500 K. A comparison of the kinetic results for the different reaction channels shows that hydrogen abstraction is strongly favored for both Vy conformers and leads to the formation of water and CH_2CHO radical. As a matter of fact, formation of Et is strongly disfavored under the harsh conditions of the ISM from both kinetic and thermodynamic points of view because of the high activation energy and strong endothermicity of the corresponding reaction path.

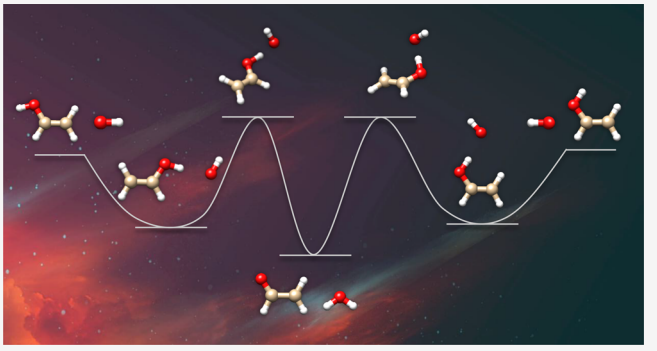

KEYWORDS: *Astrochemistry, Interstellar species, Vinyl alcohol, Reactivity, Quantum chemistry, Kinetics*

1. INTRODUCTION

A large number of studies have shown that vinyl alcohol (Vy) and hydroxyl radical (OH) are involved in various types of gas-phase processes like, for instance, the oxidation and combustion of hydrocarbons,[1] the formation of organic acids in the atmosphere and troposphere,[2] or the formation of complex organic molecules (COM) in the interstellar medium (ISM).[3] While these molecules have been identified in environments characterized by different physical−chemical conditions, the experimental procedures required for their synthesis and isolation are so challenging that a precise characterization of the chemistry of these compounds is very involved and, sometimes, even impossible.

Vy is the simplest enol and belongs to the family of C_2H_4O species, which includes also acetaldehyde and oxirane. The synthesis of Vy can be performed by a pyrolytic elimination reaction of water starting from ethylene glycol at low pressure and at a temperature of 900 K.[4] The conversion of Vy into the more stable acetaldehyde isomer is governed by a high energy barrier, but the reaction is very fast at room temperature and pressure in the presence of acid or basic catalysts. The tautomerization can also take place through a photochemical process at the low pressures and temperatures characterizing Earth's atmosphere and stratosphere.[5,6] However, under these conditions, the Vy lifetime is strongly enhanced by the synergistic effect of its intrinsic kinetic stability and the absence of chemical agents able to catalyze conversion into acetaldehyde. This situation increases, in turn, the probability of Vy reactions with other chemical species, and indeed, the involvement of Vy in the production of organic acids in the atmosphere has been demonstrated unambiguously.[7,8] These findings led da Silva et al.[9] to compute accurately the

Received: April 25, 2023
Revised: May 11, 2023
Accepted: May 22, 2023
Published: June 7, 2023

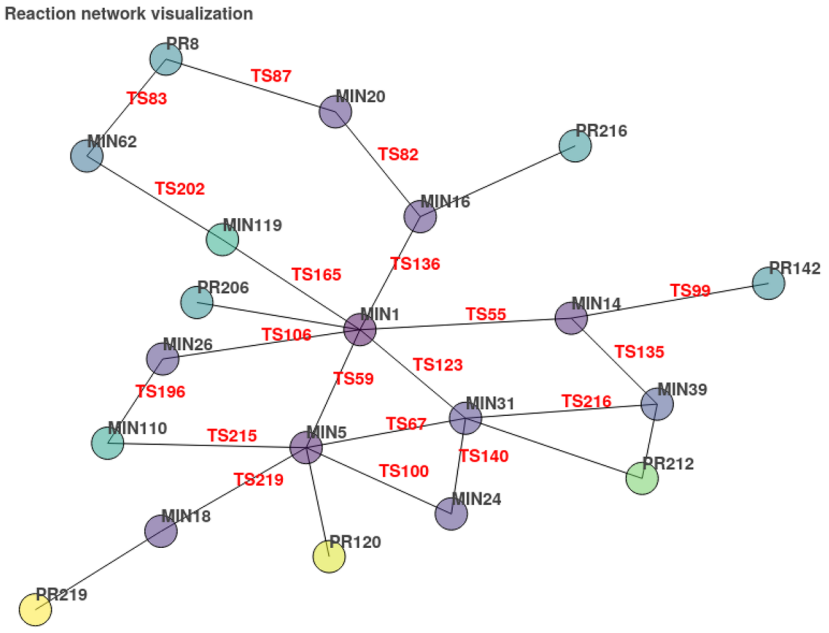

Figure 1. An example of a reaction network generated by amk_tools. The circles are the energy minima of the reaction network, while the connecting lines are the TSs.

thermodynamic properties of Vy in order to characterize its reactivity in the atmosphere with OH and molecular oxygen (O_2). In even more extreme environments, such as those characteristic of the ISM, the kinetic stability and lifetime of thermodynamically unstable species increase considerably. In fact, both conformers of Vy (*syn* and *anti*) were identified in the molecular cloud of Sagittarius B2 thanks to accurate infrared and rotational spectroscopic investigations.[10] Both conformers were recently detected also in the giant molecular cloud G+ 0.693-0.027 by Jiménez-Serra et al.,[11] who were able to derive the relative abundances and the column densities of all the members of the family of C_2H_4O compounds. Careful analysis of the spectroscopic data showed that the most stable *syn* conformer of Vy is also the most abundant one. Several reaction mechanisms involving reactions on cosmic dust, interaction with galactic cosmic rays, or the gas-phase keto−enol tautomerization of acetaldehyde have been proposed as possible formation routes of Vy.[12,13] However, neither theoretical nor experimental conclusive proofs of the viability of specific reaction mechanisms have been provided so far.

The other molecular hero of the present work is the OH radical, whose central role in combustion processes, in the chemistry of the atmosphere, in condensed-phase oxidations,[14] and in ISM formation routes has been confirmed by several studies. Indeed OH, which has been identified in the ISM already in 1963 toward Cas A,[15,16] is considered a key radical in the interstellar chemistry of oxygen, because of its ability to react with several other molecules under the harsh conditions of the ISM.[17,18] OH radical formation routes include dissociative recombinations of electrons and molecular cations formed by ion-neutral reactions (e.g., in cold interstellar clouds), photodesorption from the surface of icy grains, and, at much higher temperatures, gas-phase atom−molecule collisions like, e.g., O + H_2 and H + H_2O.[19] Photodissociation of H_2O, in the gas phase or in the mantle of icy grains, is another potential OH source.[20]

Recently, gas-phase reaction mechanisms involving Vy and the OH radical have been proposed as possible formation routes of (*Z*)-1,2-ethenediol (Et), a molecule recently detected in the ISM.[21] Et is the enolic form of glycolaldehyde and is considered a key precursor in the formation of sugars in both interstellar and prebiotic chemistry, possibly through the so-called formose reaction. Rivilla et al.[21] proposed another formation path for this molecule in the gas phase, namely the reaction between formaldehyde and hydroxyl methyl radical (CH_2OH), a species not yet identified in the ISM.

Based on these premises, we decided to perform a comprehensive study of the reaction between Vy and OH by means of a computational protocol[22] based on the generation of plausible reaction mechanisms with the help of unsupervised explorations of reactive potential energy surfaces (PES), the refinement of structural and energetic parameters by a composite quantum chemical method, and the computation of kinetic parameters (reaction rate constants and branching ratios) by the master equation (ME) approach based on ab initio transition state theory (TST). While additional reaction channels involving electron transfer would also be possible, they are beyond the scope of the present study, whose focus is the analysis of low-energy formation routes in the ISM.

The article is organized as follows. In Section 2, the computational methods are described. In Section 3, the computed reaction mechanisms are discussed with reference to the stationary points of the pertinent reactive PESs and the kinetics of all the reactions is addressed. In Section 4, the main conclusion and perspectives are summarized.

2. COMPUTATIONAL DETAILS

2.1. Reaction Mechanism Discovery. The AutoMeKin (AMK) program[23−25] was used for the unsupervised generation of plausible reaction mechanisms. Unlike other programs that require the initial optimization of the energy minima characterizing the mechanism and then the calculation of the transition states (TSs), the methodology on which AMK is built relies on the initial optimization of TS structures. Then, the connected minima are obtained from each TS by computing intrinsic reaction coordinates (IRCs).[26] In this

https://doi.org/10.1021/acsearthspacechem.3c00110
ACS Earth Space Chem. 2023, 7, 1467−1477

way, plausible reaction mechanisms can be generated by connecting all energy minima through the initially calculated TSs. In this framework, a very effective workflow is obtained in AMK by combining molecular dynamics (MD) simulations, postprocessing, and careful selection of the TS molecular structures obtained with MD.

MD simulations have been performed using the semiempirical PM7 method[27] implemented in the MOPAC software.[28] 100 trajectories per iteration were set through the keyword *ntraj* for a total of 10 iterations. The following values were set for the parameters employed by AMK to minimize the redundancy of the guess TS structures: 100 cm^{-1} for the lowest imaginary frequency (*imagmin* keyword), 0.1 for the lowest eigenvalue of the Laplacian (*eigLmax* keyword) in order to differentiate the structures resulting from the fragmentation of an intermediate, and 0.002 and 1.5 (*mapemax* and *bapemax* keywords, respectively) for the descriptors employed in the screening of the structures obtained from the MD simulations.

Optimized geometries and zero-point corrected electronic energies of reactants, TSs, intermediates, and products along the different reaction pathways were obtained using the rev-DSD-PBEP86[29]-D3BJ[30] double-hybrid functional in conjunction with the jun-cc-pVTZ basis set.[31] This combination of functional and basis set will be referred to in the following simply as rDSD. All the critical points belonging to the reaction pathways were characterized as minima (reactants, intermediates, and products) and saddle points (TSs) based on the diagonalization of analytical rDSD Hessians.[32] The nature of the minima connected by the TSs obtained in this way was determined by following IRCs at the same level of theory. Several studies have shown that this combination of functional and basis set provides accurate geometrical structures[33,34] and vibrational frequencies.[35]

The results of the simulations were analyzed using amk_tools,[36] a graphic visualizer that allows for the examination of the extremely complex reaction networks generated by AMK. A typical reaction network drawn by amk_tools is shown in Figure 1. The same software was used to visualize molecular structures with their vibrational normal modes and to check the potential energy profiles of the different reaction mechanisms. In this way it was possible to find the reaction pathways leading to the formation of all the dissociation products and to select all the structures of the critical points involved in each reaction path. For such structures, electronic energies were refined by exploiting the junChS-F12 composite scheme[37] described in more detail in the next subsection.

2.2. junChS-F12 Composite Scheme. It is widely acknowledged that the coupled-cluster (CC) model including single, double, and perturbative estimate of triple excitations (CCSD(T))[38] delivers highly accurate electronic energies for systems that do not exhibit strong multireference character, provided that complete basis set (CBS) extrapolation and core valence (CV) correlation are taken into account. The reduced cost Cheap Scheme (ChS)[37,39−41] is based on the idea that accurate CBS and CV terms can be obtained at negligible additional cost by utilizing second-order Møller−Plesset perturbation theory (MP2)[42] on top of frozen core (fc) CCSD(T) computations with (partially augmented) triple-ζ basis sets.[31,43−45] The junChS-F12 variant, in which conventional MP2 and CCSD(T) methods are replaced by their explicitly correlated (F12) counterparts,[46,47] is currently the most accurate version of the approach.[48−50] In detail

$$E_{\text{junChS-F12}} = E^{\text{CCSD(T)-F12/3Z}} + \Delta E^{\text{MP2-F12/CBS}} + \Delta E^{\text{MP2-F12/CV}} \quad (1)$$

where

$$\Delta E^{\text{MP2-F12/CBS}} = \frac{4^3 E^{\text{MP2-F12/4Z}} - 3^3 E^{\text{MP2-F12/3Z}}}{4^3 - 3^3} - E^{\text{MP2-F12/3Z}} \quad (2)$$

and

$$\Delta E^{\text{MP2-F12/CV}} = E^{\text{MP2-F12/3CZ,a.e.}} - E^{\text{MP2-F12/3CZ,f.c.}} \quad (3)$$

In eq 2, $\Delta E^{\text{MP2-F12/CBS}}$ is the MP2-F12 correlation energy extrapolated to the CBS limit by using the n^{-3} formula[51] applied to jun-cc-pVTZ (3Z) and jun-cc-pVQZ (4Z) basis sets.[43,44] Instead, the CV contribution ($\Delta E^{\text{MP2-F12/CV}}$) is incorporated as the difference between all-electron (ae) and fc MP2/F12 calculations, both with the cc-pCVTZ (3CZ) basis set.[45] The junChS-F12 energy evaluations at rDSD optimized geometries provide average absolute errors well within the so-called chemical accuracy (about 4 kJ mol^{-1}), as shown by comparison with the most accurate results available for reaction energies and activation barriers.[37,48,50] Therefore, this approach was utilized for all stationary points, together with anharmonic zero-point energy (ZPE) contributions computed in the framework of second-order vibrational perturbation theory[52] employing rDSD anharmonic force fields.

All DFT calculations were carried out using the Gaussian16 code,[53] while junChS-F12 calculations were performed using the MOLPRO program.[54−56]

2.3. Kinetics. Global and channel-specific rate constants were computed in the framework of the ab initio transition state theory based master equation approach (AITSTME), as implemented in the MESS software.[57] MESS solves the multiwell one-dimensional master equation using the chemically significant eigenvalue (CSE) method, treating bimolecular products and reactants as sources and sinks. Collisional energy relaxation was described using the exponential down model[58] with a temperature-dependent $\langle \Delta E_{\text{down}} \rangle$ of $260 \times (T/298)^{0.875}$ cm^{-1} in an argon bath. Barrierless reaction rate constants were calculated through phase space theory (PST),[59,60] approximating the long-range interaction between incoming reactants with an isotropic attractive potential $V(R) = -C_6/R^6$.[61] The C_6 parameters were obtained by a least-squares fit of rDSD electronic energies computed at different values of intermolecular distances. In Table 1 are reported the values of the C_6 parameters for all the prereactive complexes involved in the reaction mechanisms.

Rate constants of elementary steps involving distinct transition states were computed using the conventional transition-state theory. Calculations were carried out in the framework of the rigid-rotor harmonic-oscillator (RRHO) approximation and included tunneling as well as nonclassical reflection effects using the Eckart model.[62] Kinetic simulations

Table 1. C_6 Parameters in $a_0^6 E_h$ for All the Prereactive Complexes

	PrC1	PrC2	PrC4
syn	292.05	181.96	966.24
anti	30.62	123.75	29.78

https://doi.org/10.1021/acsearthspacechem.3c00110
ACS Earth Space Chem. 2023, 7, 1467−1477

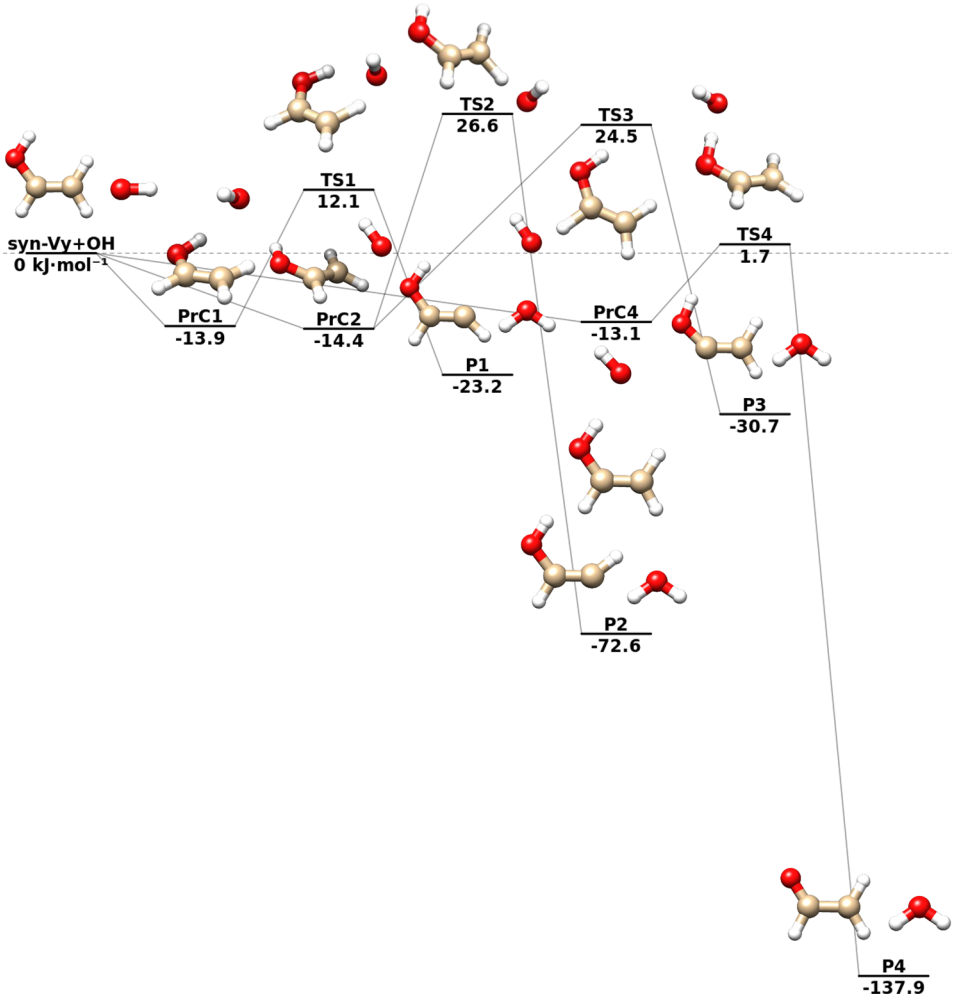

Figure 2. Energetics of the abstraction reactions between *syn*-Vy and OH: junChS-F12 energies augmented by rDSD anharmonic ZPEs. Energies are in kJ mol^{-1} relative to the reactant limit.

were performed for the conditions typical of different regions of the ISM, namely a pressure of 1×10^{-8} bar and temperatures in the range 20−500 K. The temperature dependence of the rate constants was fitted by the three-parameter Arrhenius−Kooij equation[63,64]

$$k(T) = A\left(\frac{T}{300}\right)^{n} e^{-E/RT}$$

where A, n, and E are the fitting parameters and R is the universal gas constant. The results of the kinetic analysis were further verified by calculations performed with the StarRate program, specifically designed for reactions of astrochemical interest.[65,66]

3. RESULTS

All the reaction profiles analyzed in the following subsections start with the stabilization of the reactants through non-covalent intermolecular interactions, which lead to the formation of several prereactive complexes.[67] Detailed tables in the Supporting Information report the electronic energies calculated at the junChS-F12 and rDSD levels corrected for anharmonic ZPEs calculated at the rDSD level for all the stationary points located in the different reaction paths. Although rDSD energies are not employed in the computation of thermodynamic and kinetic parameters, the fair agreement with junChS-F12 results gives further support to the use of rDSD optimized geometries and vibrational frequencies.

3.1. Mechanism of Abstraction Reactions. Hydrogen abstraction reactions from *syn*-Vy can lead to the formation of water together with four different radical species, **P1**−**P4**.

Inspection of the reaction profile in Figure 2 shows that the initial reaction step is the formation of prereactive complexes (**PrC1**, **PrC2**, or **PrC4**, lying 13.9, 14.4, and 13.1 kJ mol^{-1}, respectively, below the reactants). Starting from these prereactive complexes the reaction can further proceed through 4 different transition states, **TS1**−**TS4**, corresponding to the attack of the OH radical to the four nonequivalent hydrogen atoms of *syn*-Vy. We note that either **TS2** or **TS3** can be reached from **PrC2**, in which the OH radical forms a bifurcated hydrogen bond involving both the hydrogen atoms of the Vy CH_2 moiety.

The lowest energy barrier (**TS4**) lies 14.8 kJ mol^{-1} above the corresponding prereactive complex **PrC4** (1.7 kJ mol^{-1} above the reactants) and governs the abstraction of the hydroxyl hydrogen. The transition states ruling the other hydrogen abstractions are **TS1**−**TS3**, which lie 26.0, 41.0, and 38.9 kJ mol^{-1} above the corresponding prereactive complexes (**PrC1** and **PrC2**), respectively. The high energy barriers governing these three processes indicate that the formation of **P4** is kinetically favored. We note that the same trend would

https://doi.org/10.1021/acsearthspacechem.3c00110
ACS Earth Space Chem. 2023, 7, 1467−1477

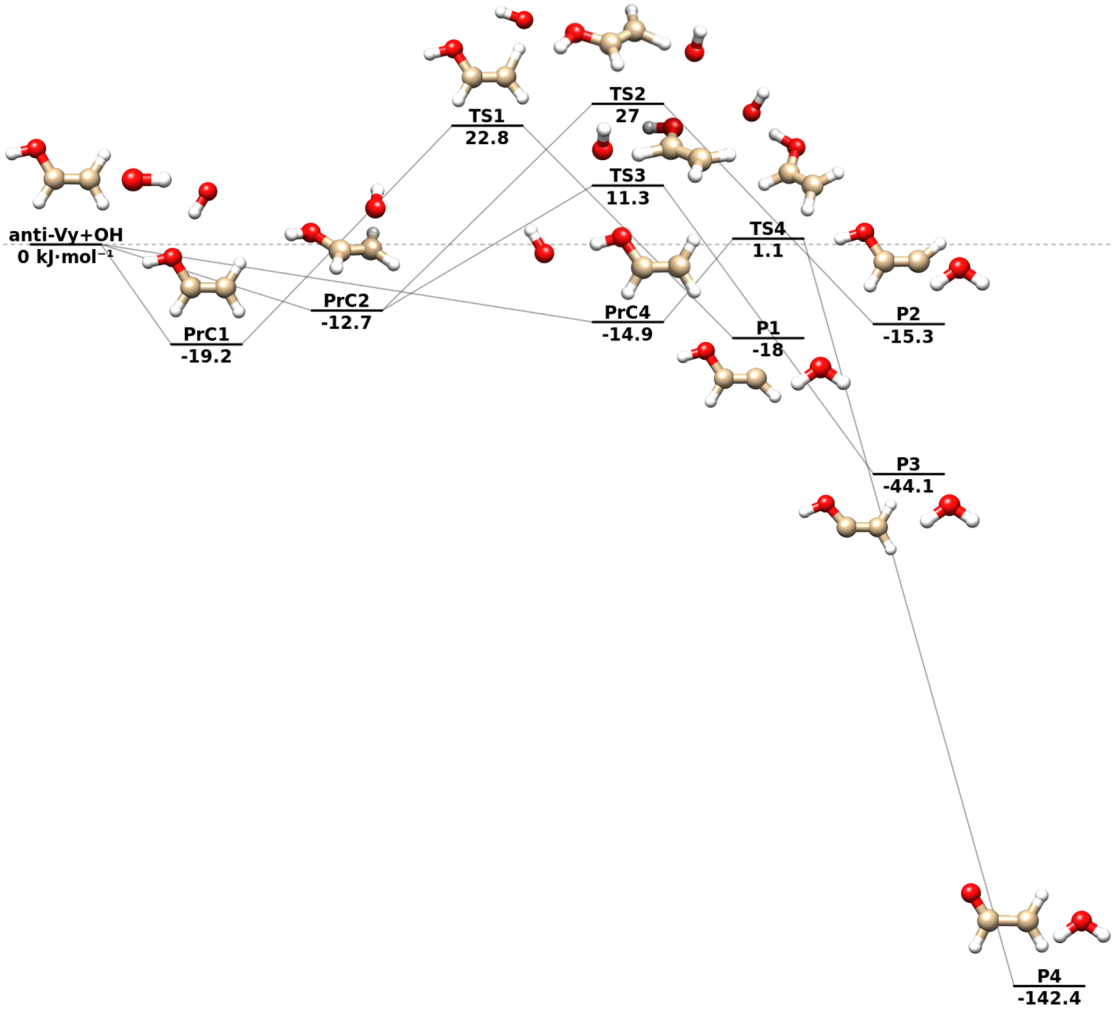

Figure 3. Energetics of the abstraction reaction between *anti*-Vy and OH: junChS-F12 energies augmented by rDSD anharmonic ZPEs. Energies are in kJ mol^{-1} relative to the reactant limit.

be obtained in terms of thermodynamic control since **P4** lies −137.9 kJ mol^{-1} below the reactants, whereas the exothermicity of the reactions leading to **P1**−**P3** are 23.2, 72.6, and 30.7 kJ mol^{-1}, respectively. The preference for the route leading to **P4** can be traced back to the lower strength of the OH bond with respect to its CH counterparts and to the stabilization of the CH_2CHO radical by π-electron delocalization in the C−C−O moiety.

In analogy with the case of *syn*-Vy, also the abstraction reactions involving the *anti* conformer start with the stabilization of the initial reagents through the formation of a prereactive complex (**PrC1**, **PrC2**, or **PrC4**).

The most stable complex is **PrC1**, which lies 19.2 kJ mol^{-1} below the reactants, whereas **PrC2** and **PrC4** lie 12.7 and 14.9 kJ mol^{-1}, respectively, below the reactants. The reaction then proceeds through the attack of OH to one of the hydrogen atoms of *anti*-Vy, overcoming the corresponding transition state (**TS1**, **TS2**, **TS3**, or **TS4**). Inspection of the energy barriers collected in Figure 3 shows that the favored abstraction process leads to the formation of **P4** following the **PrC4** → **TS4** → **P4** path. In fact, **TS4** is found 1.1 kJ mol^{-1} above the reactants, whereas **TS1**−**TS3** lie 22.8, 27.0, and 11.3 kJ mol^{-1} above the reactants. All the reactions are exothermic, but all the paths except that leading to **P4** are governed by energy barriers higher than 10 kJ mol^{-1}. As a consequence, the reactants would have to acquire from the surrounding environment a significant energy, with this being a highly unlikely process under the harsh conditions of the ISM.

3.2. Mechanism of Addition Reactions. The initial step of all the addition reactions of OH to *syn*-Vy is the formation of the same prereactive complex (**PrC1**) already discussed for the corresponding abstraction reactions, which lies 13.9 kJ mol^{-1} below the reactants.

Next, the OH radical can attack one of the two ends of the C═C double bond overcoming either the **TS1** or **TS2** transition state, which lie 9.6 and 6.1 kJ mol^{-1}, respectively, below the reactants. Then, the reaction intermediate **IM1** or **IM2** can be formed by strongly exothermic processes (117.1 or 131.7 kJ mol^{-1}, respectively, below the reactants). Several reactive pathways start from these two intermediates, corresponding to isomerization and dissociation reactions leading to the formation of molecules not yet detected in the ISM, but also to already identified species. In detail, the reaction can proceed through the isomerization reaction by transposition of hydrogen from **IM1** to **IM3** or from **IM2** to **IM4**, with **IM3** (71.5 kJ mol^{-1} below the reactants) and **IM4** (116.8 kJ mol^{-1} below the reactants) being less stable than the other two intermediates. These processes are governed by the two transition states **TS1GA** and **TS2GA**, which lie 41.6 and 20.6 kJ mol^{-1}, respectively, above the reactants. Two other

https://doi.org/10.1021/acsearthspacechem.3c00110
ACS Earth Space Chem. 2023, 7, 1467−1477

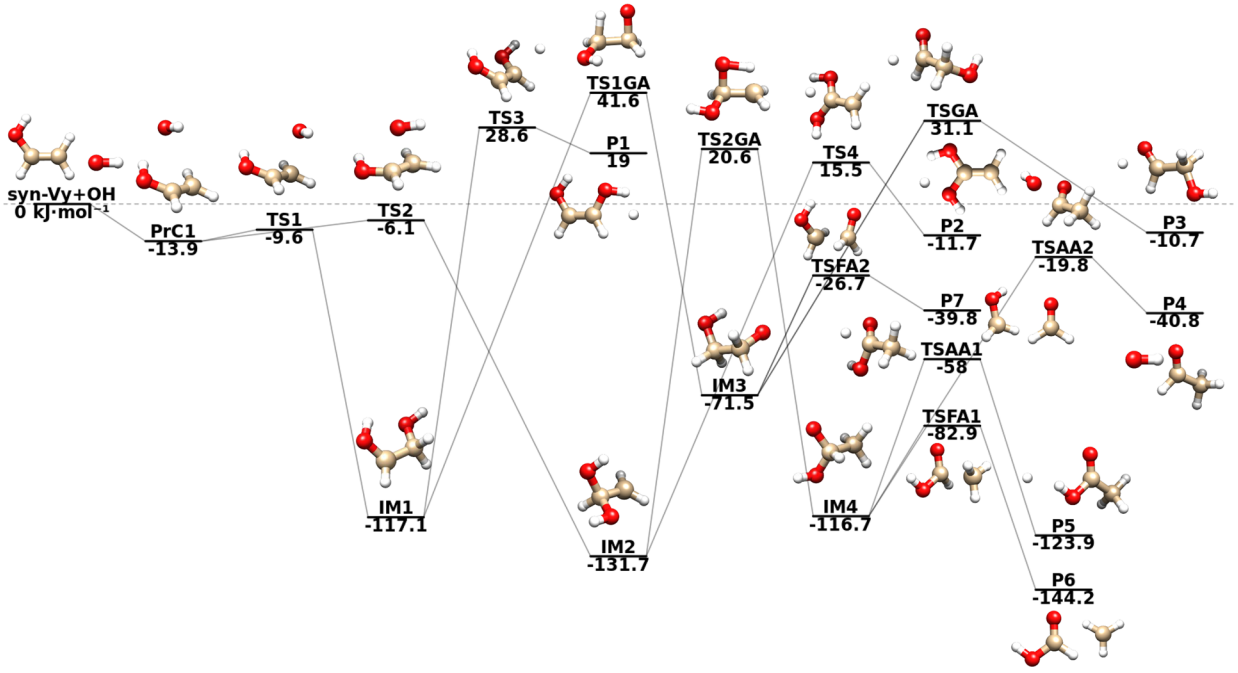

Figure 4. Energetics of the addition reactions between *syn*-Vy and OH: junChS-F12 energies augmented by rDSD anharmonic ZPEs. Energies are in kJ mol^{-1} relative to the reactant limit.

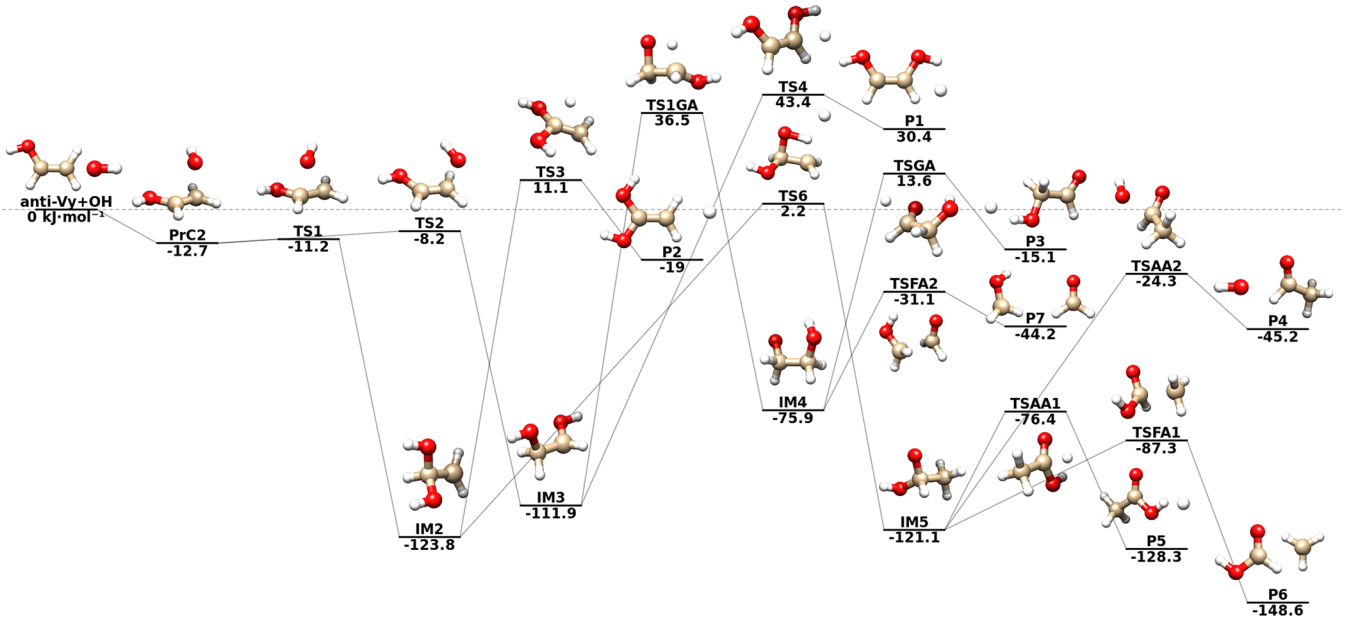

Figure 5. Energetics of the addition reactions between *anti*-Vy and OH: junChS-F12 energies augmented by rDSD anharmonic ZPEs. Energies are in kJ mol^{-1} relative to the reactant limit.

reactive pathways can be followed starting from **IM1** and **IM2**, namely the dissociation reactions which lead to the formation of the 1,2 (**P1**)- and 1,1 (**P2**)-isomers of ethenediol shown in Figure 4, overcoming the corresponding transition states **TS3** and **TS4**, which lie 28.6 and 15.5 kJ mol^{-1}, respectively, above the reactants. However, formation of **P1** in the ISM is unlikely in view of the non-negligible endothermicity (19.0 kJ mol^{-1}) of the reaction. On the other hand, **P2** lies below the asymptotic limit of the reactants by about 11.7 kJ mol^{-1}. Then, dissociation of **IM3** and **IM4** can lead to a hydroxymethyl radical and formaldehyde (**P7**), formic acid and methyl radical (**P6**), acetic acid and atomic hydrogen (**P5**), acetaldehyde and hydroxyl radical (**P4**), or glycolaldehyde and atomic hydrogen (**P3**). While all these processes are exothermic, the high energy of the corresponding transition states (**TS1GA**, **TS2GA**, **TSGA**) indicate that these reaction channels are closed under the typical ISM conditions.

The first step of all addition reactions involving the *anti*-Vy conformer is the formation of the same prereactive complex (**PrC2**) already discussed for the corresponding abstraction reactions and lying 12.7 kJ mol^{-1} below the reactants.

The reactions then proceed with the attack of the OH radical to the double bond of Vy, which can lead to the formation of two different reaction intermediates, **IM2** or **IM3**,

https://doi.org/10.1021/acsearthspacechem.3c00110
ACS Earth Space Chem. 2023, 7, 1467−1477

lying 123.8 and 111.9 kJ mol^{-1}, respectively, below the reactants. Next, **IM2** can isomerize to **IM5** through **TS6**, and **IM3** can isomerize to **IM4** through **TS1GA**. Inspection of Figure 5 shows that the **IM2** → **TS6** → **IM5** channel is the favored one, since it involves energy barriers significantly lower than those governing the alternative pathway leading to the formation of **P2**. Starting from **IM5**, acetaldehyde (**P4**), acetic acid (**P5**), or formic acid (**P6**) can be produced through the transition states **TSAA2**, **TSAA1**, and **TSFA1**, which lie respectively 24.3, 76.4, and 87.3 kJ mol^{-1} below the reactants. Two other dissociation pathways have been identified, which start from the higher energy intermediate **IM4** and lead to the formation of glycolaldehyde (**P3**) through a hydrogen elimination process governed by an energy barrier of 13.6 kJ mol^{-1} above the reactants (**TSGA**) or to the formation of formic acid (**P7**) through **TSFA2**, which lies 31.1 kJ mol^{-1} below the asymtotic limit. Also in this case all the reaction channels shown in Figure 5 are unlikely to be open in the ISM in view of the high energy barriers (well above the asymptotic limit of the reactants) to be overcome.

3.3. Rate Constants. The rate constants for the abstraction and addition reactions of both Vy conformers are depicted as Arrhenius plots in Figure 6−9 in order to give a better and more comprehensible graphical representation of the kinetic results. In Tables 2−5 are collected the parameters of the corresponding Arrhenius−Kooij fits.

Starting from abstraction reactions involving *syn*-Vy, inspection of the results reported in Figure 6 and Table 2 shows that the rate constant governing the formation of **P4** (which ranges between 1.40 × 10^{-12} and 3.70 × 10^{-11} cm^3 molecule^{-1} s^{-1}) is higher than the rate constants governing the formation of **P1**−**P3** in the whole interval of temperatures (20−500 K). This trend parallels that of the energy barriers involved in the reaction pathways leading to the various products, which are all single-step reactions. In fact, the energy barrier governing the formation of **P4** is 14.8 kJ mol^{-1}, to be compared to values of 26.0, 38.9, and 41.0 kJ mol^{-1} for the channels leading to **P1**, **P3**, and **P2**, respectively. In agreement with those barriers, the second most kinetically favored single-step reaction pathway is **PrC1**−**TS1**−**P1**, whose rate constant ranges between 1.40 × 10^{-14} and 9.63 × 10^{-13} cm^3 molecule^{-1} s^{-1}. The rate constant for the reaction channel leading to **P3** ranges between 4.20 × 10^{-15} and 2.25 × 10^{-13} cm^3 molecule^{-1} s^{-1}. Finally, the rate constant governing the formation of **P2** ranges between 3.20 × 10^{-16} and 1.68 × 10^{-14} cm^3 molecule^{-1} s^{-1}.

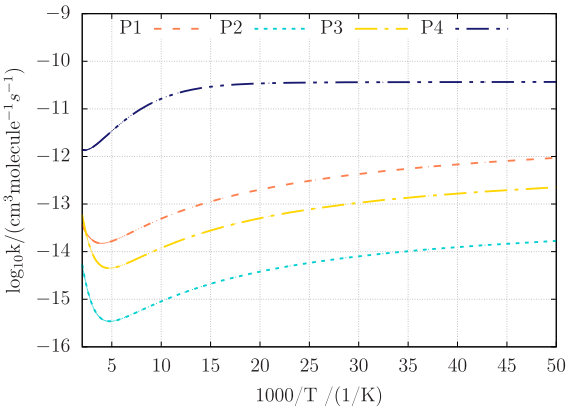

Figure 6. Arrhenius plot of the rate constants for the abstraction reactions involving *syn*-Vy and OH leading to **P1**−**P4**.

Table 2. Arrhenius−Kooij Parameters for the Abstraction Reactions Involving *syn*-Vy

	A/cm^3 molecule^{-1} s^{-1}	n	E/kJ mol^{-1}	rms[a]
P1	9.49 × 10^{-1}	2.66	459.65	1.42 × 10^{-15}
P2	1.43 × 10^{10}	3.05	20084.77	4.97 × 10^{-17}
P3	6.80 × 10^{9}	3.02	20270.54	1.19 × 10^{-15}
P4	1.21 × 10^{-11}	2.19	−1382.16	2.82 × 10^{-14}

[a]rms stands for root-mean-square deviation of the fit.

Figure 7 and Table 3 show that also for the abstraction reactions involving the *anti* isomer the fastest process leads to the formation of **P4** in the whole interval of temperatures (20−500 K) and its rate constant ranges between 8.8 × 10^{-13} and 2.50 × 10^{-11} cm^3 molecule^{-1} s^{-1}. Once again the trend of rate constants parallels that of energy barriers. Accordingly, the second highest rate constant (ranging between 5.80 × 10^{-14} and 2.90 × 10^{-12} cm^3 molecule^{-1} s^{-1}) governs the formation of **P3**, with the barrier associated to this abstraction process being about 24.0 kJ mol^{-1}. Next, formation of **P1** is governed by an energy barrier of 42.0 kJ mol^{-1} and its rate constant ranges between 1.70 × 10^{-15} and 8.38 × 10^{-14} cm^3 molecule^{-1} s^{-1}.

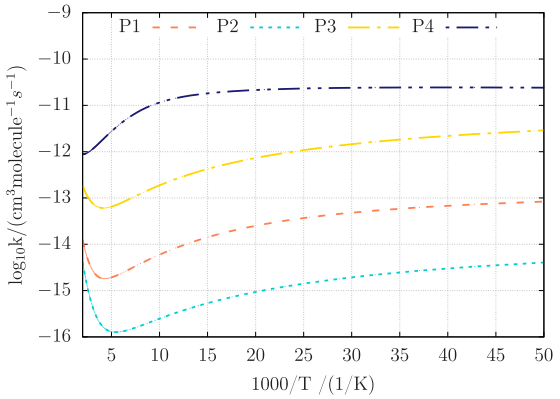

Figure 7. Arrhenius plot of the rate constants for the abstraction reactions involving *anti*-Vy and OH leading to **P1**−**P4**.

Table 3. Arrhenius−Kooij Parameters for the Abstraction Reactions Involving *anti*-Vy

	A/cm^3 molecule^{-1} s^{-1}	n	E/kJ mol^{-1}	rms[a]
P1	4.03 × 10^{8}	3.01	16428.82	9.95 × 10^{-17}
P2	3.79 × 10^{11}	3.03	20379.33	9.42 × 10^{-17}
P3	1.44 × 10^{-2}	2.94	5147.99	8.46 × 10^{-16}
P4	2.35 × 10^{-11}	1.86	−1454.88	3.02 × 10^{-14}

[a]rms stands for root-mean-square deviation of the fit.

Finally, the slowest process is the formation of **P2**, which is ruled by an energy barrier of 39.7 kJ mol^{-1} and has a rate constant ranging between 1.15 × 10^{-16} and 4.13 × 10^{-15} cm^3 molecule^{-1} s^{-1}. We note that the energy barrier governing the formation of **P2** is actually lower than that of **P1**, but the corresponding transition states are reached from two different intermediates (**PrC2** and **PrC1**), so that **TS2** is less stable than **TS1** with respect to the energy of the reactants. At the low pressures characterizing the ISM, the excess energy of prereactive complexes cannot be dissipated by intermolecular interactions with the surrounding gas, so that the correct

https://doi.org/10.1021/acsearthspacechem.3c00110
ACS Earth Space Chem. 2023, 7, 1467−1477

energy reference is that of reactants. This point is further analyzed in the General Discussion section.

Coming to addition reactions, the results reported in Figure 8 and Table 4 show that in the whole interval of temperatures

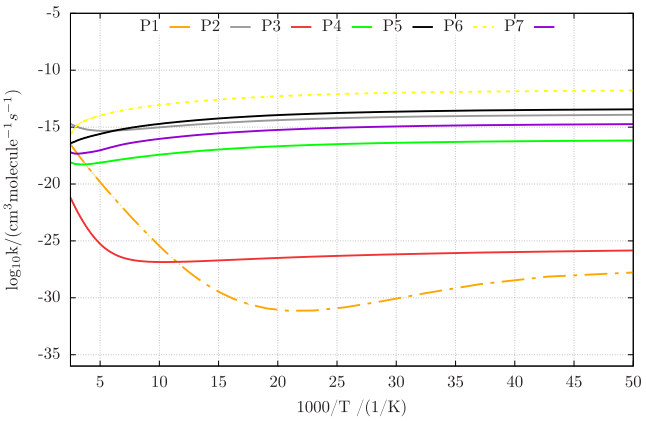

Figure 8. Arrhenius plots of the constants for the addition reactions involving *syn*-Vy and OH leading to **P1**−**P7**.

Table 4. Arrhenius−Kooij Parameters for the Addition Reactions Involving *syn*-Vy

	A/cm^3 molecule^{-1} s^{-1}	n	E/kJ mol^{-1}	rms[a]
P1	5.42×10^{-10}	3.31	18097.41	7.54×10^{-19}
P2	8.09×10^{-3}	2.54	8222.08	2.83×10^{-18}
P3	1.10×10^{13}	6.94	28929.39	1.99×10^{-23}
P4	1.99	5.06	8305.40	9.42×10^{-22}
P5	2.95×10^{4}	2.64	12223.05	2.54×10^{-20}
P6	3.86×10^{5}	1.20	15365.07	4.29×10^{-19}
P7	1.30×10^{23}	4.52	20867.25	6.13×10^{-20}

[a]rms stands for root-mean-square deviation of the fit.

(20−500 K) the formation of **P6** is governed by the highest rate constant, which ranges between 2.10×10^{-16} and 1.66×10^{-12} cm^3 molecule^{-1} s^{-1}. All the other products are formed by multistep reaction pathways governed by rate constants decreasing in the order **P5** > **P2** > **P7** > **P4**. The slowest reaction channel leads to the formation of Et (**P1**), whose rate constant ranges between 1.70×10^{-30} and 1.82×10^{-16} cm^3 molecule^{-1} s^{-1} in the whole temperature range. This finding is related both to the significant endothermicity of the process (30.4 kJ mol^{-1}) and to the presence of the highest energy barrier (**TS4**, 43.4 kJ mol^{-1}). A small rate constant characterizes also the reaction channel leading to **P3** (between 1.04×10^{-27} and 1.09×10^{-20}c m^3 molecule^{-1} s^{-1}), which, despite being exothermic (15.1 kJ mol^{-1}), is a multistep process involving a high energy barrier for the rate-determining step (**TS1GA**, 36.5 kJ mol^{-1}).

While the general trend of the rate constants governing addition reactions to *anti*-Vy is analogous to that of the *syn* isomer, the reaction pathways discovered by AutoMeKin involve different energy barriers, which lead to non-negligible quantitative differences. In any case, the results reported in Figure 9 and Table 5 show that in the whole temperature interval the highest rate constant (between 2.00×10^{-13} and 1.01×10^{-11} cm^3 molecule^{-1} s^{-1}) governs again the formation of **P6**, while the formation of 1,1- and 1,2-ethenediol isomers (**P1** and **P2**, respectively) is kinetically disadvantaged. In particular, the rate constant for the formation of **P1** ranges

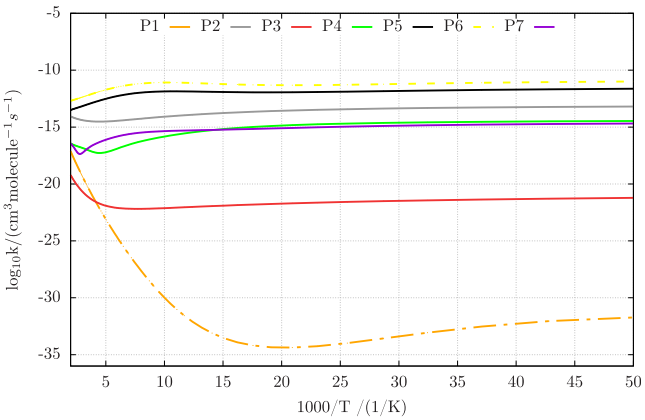

Figure 9. Arrhenius plots of the rate constants for the addition reactions involving *anti*-Vy and OH leading to **P1**−**P7**.

Table 5. Arrhenius−Kooij Parameters for the Addition Reactions Involving *anti*-Vy

	A/cm^3 molecule^{-1} s^{-1}	n	E/kJ mol^{-1}	rms[a]
P1	8.93×10^{-7}	2.61	36638.56	1.84×10^{-20}
P2	9.78×10^{-7}	2.39	3740.35	6.36×10^{-18}
P3	1.00×10^{12}	4.85	25123.29	5.77×10^{-23}
P4	9.78×10^{-14}	5.36	−9872.98	4.11×10^{-20}
P5	$1{,}04 \times 10^{-13}$	1.51	−3746.10	1.60×10^{-17}
P6	8.89×10^{-13}	0.86	−2477.75	6.02×10^{-17}
P7	7.01×10^{17}	3.03	21657.89	6.94×10^{-20}

[a]rms stands for root-mean-square deviation of the fit.

between 1.10×10^{-34} and 7.40×10^{-18} cm^3 molecule^{-1} s^{-1}, whereas that of **P2** ranges between 2.9×10^{-15} and 6.3×10^{-14} cm^3 molecule^{-1} s^{-1}.

4. GENERAL DISCUSSION AND CONCLUSIONS

Vinyl alcohol has two conformers (*syn* and *anti*) with a computed energy difference of 4.7 kJ mol^{-1} and an interconversion barrier lying 18.0 kJ mol^{-1} above the more stable (*syn*) species. Both conformers have been detected in different regions of the ISM, and the observed relative populations (8.3/1)[10,11] agree with their computed counterparts at temperatures close to 60 K. These findings suggest that interconversion between the conformers is unlikely. Furthermore, only one structure exists for CH_2CHO (**P4**), whereas *syn* and *anti* conformers are possible for other intermediates and products. In particular, the *syn* conformer of Et (**P1** in Figure 4) is more stable than its *anti* counterpart (**P1** in Figure 5) by 16.1 kJ mol^{-1}.

The results of the previous sections show unambiguously that hydrogen abstraction reactions are kinetically favored with respect to additions and lead preferentially to the formation of the CH_2CHO radical (**P4**) from both vinyl alcohol conformers. The reaction channels leading to formation of Et (**P1** in Figures 4 and 5) turn out to be the most kinetically disadvantaged, in agreement with the endothermicity of the corresponding reactions. In analogy with the reaction of OH with saturated alcohols,[68,69] the addition reaction (producing in the present case formic acid and methyl radical, **P6**) becomes competitive with the abstraction reaction at high temperatures. However, this feature is not significant for the ISM regions, which are the reference environments in the present investigation. While some of the reaction channels

https://doi.org/10.1021/acsearthspacechem.3c00110
ACS Earth Space Chem. 2023, 7, 1467−1477

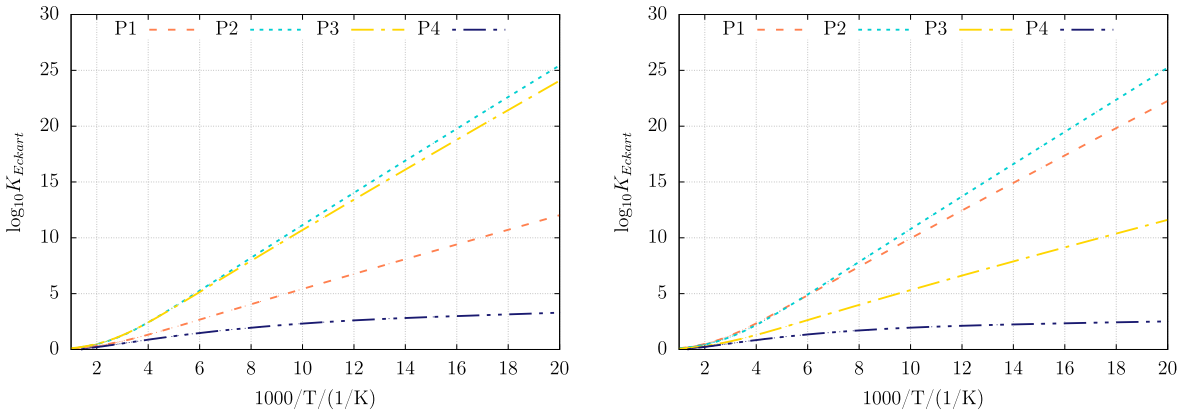

Figure 10. Eckart tunneling coefficients as a function of temperature for the abstraction reactions involving the *syn* conformer on the left and the *anti* conformer on the right.

starting from the *anti* conformer are marginally faster than those starting from the *syn* conformer, this finding has no consequence on the general trends due to the small quantitative difference and the negligible initial population of the *syn* conformer (about 10% at 60 K, as mentioned above).

Since all the reaction paths involve emerged energy barriers, these channels can be open at the low temperatures of the ISM only in the presence of effective tunneling contributions. From an analysis of the tunneling coefficients calculated with the Eckart model for the hydrogen abstraction processes of both *syn* and *anti* conformers shown in Figure 10, it is apparent that tunneling plays a dominant role in the range of temperatures characteristic of the ISM (typically between 50 and 200 K) and then decays very rapidly for temperatures higher than about 200 K. Furthermore, the rate constants governing the formation of all the products have a negative dependence on the temperature in the very low pressure and temperature regime. As already addressed by Guo et al.[68] and Zheng et al.,[69] always in the context of hydrogen abstraction reactions, this is due to the lack of collisional stabilization of the prereactive complex. Indeed, as shown in Figure 11, for

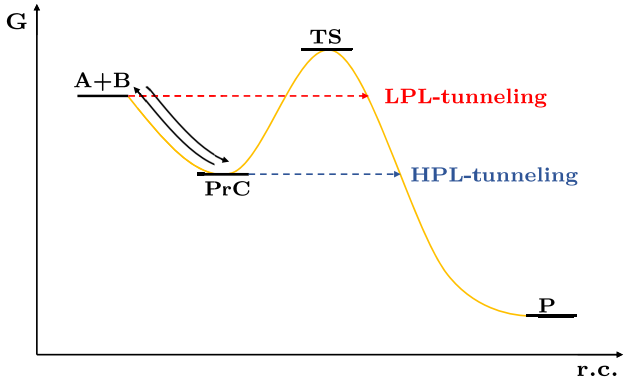

Figure 11. Representation of the low-temperature kinetics for high- and low-pressure limits (HPL and LPL, respectively).

sufficiently high pressures the stabilization of the prereactive complex is favored, with this allowing deep tunneling starting from its zero-point energy and leading, at the same time, to an increase of the rate constant with the temperature. However, in the absence of stabilizing collisions (as is the case for very low pressures) tunneling can take place only at energies above that of the reagents, with this limitation reducing the value of the rate constant with respect to its high-pressure counterpart. Indeed, in such a situation, rate constants approach the value of the capture rate constant for the formation of the prereactive complex from the initial reagents.

While the treatment of tunneling employed in the present study (zero-curvature model based on an Eckart potential) delivers qualitatively correct results, quantitative computation would require more advanced models.[70] However, these refinements are outside the scope of the present paper, which is mainly devoted to the analysis of possible formation routes of Et at low pressures and temperatures. In this framework, the predominance of abstraction over addition with the consequent preferential formation of the CH_2CHO radical (**P4**) over Et (**P1**) has been proven beyond any reasonable doubt. Therefore, we suggest to search for this radical species in the ISM regions where Vy and OH have been detected, i.e. Sagittarius B2 and G+ 0.693-0.027.

Our analysis led to the identification among the possible products of a couple of reactants, formaldehyde and hydroxymethyl radical (**P7**), suggested by Rivilla et al.[21] as possible precursors of Et. However, also the reaction leading from **P7** to **P1** is endothermic (by about 30 kJ mol^{-1}) and, therefore, unlikely to be feasible under the conditions of the ISM. Therefore, the results of our computational study suggest the search of alternative reactions in the gas phase able to produce Et or the investigation of possible formation routes on grain surfaces.

Together with the intrinsic interest of the studied formation routes, the computational strategy proposed in the present study paves the way toward systematic investigations of reaction paths for complex organic molecules in the interstellar medium by effective user-friendly tools.

■ ASSOCIATED CONTENT

Supporting Information

The Supporting Information is available free of charge at https://pubs.acs.org/doi/10.1021/acsearthspacechem.3c00110.

Cartesian coordinates and relative energies of all critical points, plots of the barrierless reaction steps, and MESS input files (PDF)

https://doi.org/10.1021/acsearthspacechem.3c00110
ACS Earth Space Chem. 2023, 7, 1467−1477

AUTHOR INFORMATION

Corresponding Authors

Bernardo Ballotta − *Scuola Normale Superiore, 56126 Pisa, Italy;* orcid.org/0000-0002-1591-9189; Email: bernardo.ballotta@sns.it

Vincenzo Barone − *Scuola Normale Superiore, 56126 Pisa, Italy;* orcid.org/0000-0001-6420-4107; Email: vincenzo.barone@sns.it

Authors

Emilio Martínez-Núñez − *Departamento de Química Física, Facultade de Química, Campus Vida, Universidade de Santiago de Compostela, 15782 Santiago de Compostela, Spain;* orcid.org/0000-0001-6221-4977

Sergio Rampino − *Università degli Studi di Padova, Dipartimento di Scienze Chimiche, 35131 Padova, Italy; Istituto Nazionale di Fisica Nucleare, Sezione di Pisa, 56127 Pisa, Italy;* orcid.org/0000-0001-8525-7777

Complete contact information is available at: https://pubs.acs.org/10.1021/acsearthspacechem.3c00110

Notes

The authors declare no competing financial interest.

ACKNOWLEDGMENTS

Funding from the Italian Ministry of University and Research (MUR, Grant 2017A4XRCA) and Italian Space Agency (ASI, "Life in Space" project No. 2019-3-U.0) is gratefully acknowledged. This work was partially supported by the Consellería de Cultura, Educación e Ordenación Universitaria (Grupo de referencia competitiva ED431C 2021/40) and the Ministerio de Ciencia e Innovación through Grant # PID2019-107307RB-I00. We acknowledge the "Centro de Supercomputación de Galicia" (CESGA) for the use of computer facilities.

REFERENCES

(1) Cool, T. A.; Nakajima, K.; Mostefaoui, T. A.; Qi, F.; McIlroy, A.; Westmoreland, P. R.; Law, M. E.; Poisson, L.; Peterka, D. S.; Ahmed, M. Selective detection of isomers with photoionization mass spectrometry for studies of hydrocarbon flame chemistry. *J. Chem. Phys.* **2003**, *119*, 8356−8365.

(2) Archibald, A. T.; McGillen, M. R.; Taatjes, C. A.; Percival, C. J.; Shallcross, D. E. Atmospheric transformation of enols: A potential secondary source of carboxylic acids in the urban troposphere. *Geophys. Res. Lett.* **2007**, *34*, 1.

(3) Abplanalp, M. J.; Gozem, S.; Krylov, A. I.; Shingledecker, C. N.; Herbst, E.; Kaiser, R. I. A study of interstellar aldehydes and enols as tracers of a cosmic ray-driven nonequilibrium synthesis of complex organic molecules. *Proc. Nat. Acad. Sci.* **2016**, *113*, 7727−7732.

(4) Clayden, J.; Greeves, N.; Warren, S. *Organic Chemistry*, 2nd ed.; Oxford University Press: 2012.

(5) Heazlewood, B.; Maccarone, A.; Andrews, D.; et al. Near-threshold H/D exchange in CD3CHO photodissociation. *Nature Chem.* **2011**, *3*, 443−448.

(6) Andrews, D. U.; Heazlewood, B. R.; Maccarone, A. T.; Conroy, T.; Payne, R. J.; Jordan, M. J. T.; Kable, S. H. Photo-Tautomerization of Acetaldehyde to Vinyl Alcohol: A Potential Route to Tropospheric Acids. *Science* **2012**, *337*, 1203−1206.

(7) Lei, X.; Wang, W.; Gao, J.; Wang, S.; Wang, W. Atmospheric Chemistry of Enols: The Formation Mechanisms of Formic and Peroxyformic Acids in Ozonolysis of Vinyl Alcohol. *J. Phys. Chem. A* **2020**, *124*, 4271−4279.

(8) So, S.; Wille, U.; da Silva, G. Atmospheric Chemistry of Enols: A Theoretical Study of the Vinyl Alcohol + OH + O2 Reaction Mechanism. *Environ. Sci. Technol.* **2014**, *48*, 6694−6701.

(9) da Silva, G.; Kim, C.-H.; Bozzelli, J. W. Thermodynamic Properties (Enthalpy, Bond Energy, Entropy, and Heat Capacity) and Internal Rotor Potentials of Vinyl Alcohol, Methyl Vinyl Ether, and Their Corresponding Radicals. *J. Phys. Chem. A* **2006**, *110*, 7925−7934.

(10) Turner, B. E.; Apponi, A. J. Microwave Detection of Interstellar Vinyl Alcohol, CH2 = CHOH. *Astrophys. J.* **2001**, *561*, L207.

(11) Jiménez-Serra, I.; Rodríguez-Almeida, L. F.; Martín-Pintado, J.; Rivilla, V. M.; Melosso, M.; Zeng, S.; Colzi, L.; Kawashima, Y.; Hirota, E.; Puzzarini, C.; Tercero, B.; de Vicente, P.; Rico-Villas, F.; Requena-Torres, M. A.; Martín, S. Precursors of fatty alcohols in the ISM: Discovery of n-propanol. *Astron. Astrophys.* **2022**, *663*, A181.

(12) Kleimeier, N. F.; Kaiser, R. I. Interstellar Enolization-Acetaldehyde (CH3CHO) and Vinyl Alcohol (H2CCH(OH)) as a Case Study. *Chem. Phys. Chem.* **2021**, *22*, 1229−1236.

(13) Peeters, J.; Nguyen, V. S.; Müller, J.-F. Atmospheric Vinyl Alcohol to Acetaldehyde Tautomerization Revisited. *J. Phys. Chem. Lett.* **2015**, *6*, 4005−4011.

(14) Alberto, M. E.; Russo, N.; Grand, A.; Galano, A. A physicochemical examination of the free radical scavenging activity of Trolox: mechanism, kinetics and influence of the environment. *Phys. Chem. Chem. Phys.* **2013**, *15*, 4642−4650.

(15) Barrett, A. H. Radio Observations of Interstellar Hydroxyl Radicals. *Science* **1967**, *157*, 881−889.

(16) Weinreb, S.; Barrett, A. H.; Meeks, M. L.; Henry, J. C. *97. Radio Observations of OH in the Interstellar Medium*; Harvard University Press: 1979; pp 666−670.

(17) Hollenbach, D.; McKee, C. F. Molecule formation and infrared emission in fast interstellar shocks. I Physical processes. *Astrophys. J. Suppl. Ser.* **1979**, *41*, 555−592.

(18) Neufeld, D. A.; Dalgarno, A. Fast molecular shocks. I-Reformation of molecules behind a dissociative shock. *Astrophys. J.* **1989**, *340*, 869−893.

(19) Van Dishoeck, E. F.; Herbst, E.; Neufeld, D. A. Interstellar water chemistry: from laboratory to observations. *Chem. Rev.* **2013**, *113*, 9043−9085.

(20) Chang, Y.; Yu, Y.; Wang, H. Hydroxyl super rotors from vacuum ultraviolet photodissociation of water. *Nature Commun.* **2019**, *10*, 1250.

(21) Rivilla, V. M.; et al. Precursors of the RNA World in Space: Detection of (Z)-1,2-ethenediol in the Interstellar Medium, a Key Intermediate in Sugar Formation. *Astrophys. J. Lett.* **2022**, *929*, L11.

(22) Ballotta, B.; Marforio, T. D.; Rampino, S.; Martínez-Núñez, E.; Barone, V.; Melosso, M.; Bottoni, A.; Dore, L. Toward the Detection of Cyanoketene in the Interstellar Medium: New Hints from Quantum Chemistry and Rotational Spectroscopy. *ACS Earth Space Chem.* **2023**, *7*, 1172−1180.

(23) Martínez-Núñez, E. An automated method to find transition states using chemical dynamics simulations. *J. Comput. Chem.* **2015**, *36*, 222−234.

(24) Martínez-Núñez, E. An automated transition state search using classical trajectories initialized at multiple minima. *Phys. Chem. Chem. Phys.* **2015**, *17*, 14912−14921.

(25) Martínez-Núñez, E.; Barnes, G. L.; Glowacki, D. R.; Kopec, S.; Peláez, D.; Rodríguez, A.; Rodríguez-Fernández, R.; Shannon, R. J.; Stewart, J. J. P.; Tahoces, P. G.; Vazquez, S. A. AutoMeKin2021: An open-source program for automated reaction discovery. *J. Comput. Chem.* **2021**, *42*, 2036−2048.

(26) Fukui, K. The path of chemical reactions - the IRC approach. *Acc. Chem. Res.* **1981**, *14*, 363−368.

(27) Stewart, J. J. P. Optimization of parameters for semiempirical methods VI: more modifications to the NDDO approximations and re-optimization of parameters. *J. Mol. Model.* **2013**, *19*, 1−32.

(28) Stewart, J. J. P. *MOPAC2016*.

(29) Kozuch, S.; Martin, J. M. L. DSD-PBEP86: in search of the best double-hybrid DFT with spin-component scaled MP2 and dispersion corrections. *Phys. Chem. Chem. Phys.* **2011**, *13*, 20104−20107.

(30) Grimme, S.; Ehrlich, S.; Goerigk, L. Effect of the damping function in dispersion corrected density functional theory. *J. Comput. Chem.* **2011**, *32*, 1456−1465.
(31) Papajak, E.; Zheng, J.; Xu, X.; Leverentz, H. R.; Truhlar, D. G. Perspectives on Basis Sets Beautiful: Seasonal Plantings of Diffuse Basis Functions. *J. Chem. Theory. Comput.* **2011**, *7*, 3027−3034.
(32) Biczysko, M.; Panek, P.; Scalmani, G.; Bloino, J.; Barone, V. Harmonic and Anharmonic Vibrational Frequency Calculations with the Double-Hybrid B2PLYP Method: Analytic Second Derivatives and Benchmark Studies. *J. Chem. Theory. Comput.* **2010**, *6*, 2115−2125.
(33) Ceselin, G.; Barone, V.; Tasinato, N. Accurate Biomolecular Structures by the Nano-LEGO Approach: Pick the Bricks and Build Your Geometry. *J. Chem. Theory Comput.* **2021**, *17*, 7290−7311.
(34) Barone, V.; Fusè, M.; Lazzari, F.; Mancini, G. Benchmark Structures and Conformational Landscapes of Amino Acids in the Gas Phase: a Joint Venture of Machine Learning, Quantum Chemistry, and Rotational Spectroscopy. *J. Chem. Theory Comput.* **2023**, *19*, 1243−1260.
(35) Barone, V.; Ceselin, G.; Fusè, M.; Tasinato, N. Accuracy meets interpretability for computational spectroscopy by means of hybrid and double-hybrid functionals. *Front. Chem.* **2020**, *8*, 584203.
(36) Garay-Ruiz, D.; Álvarez Moreno, M.; Bo, C.; Martínez-Núñez, E. New Tools for Taming Complex Reaction Networks: The Unimolecular Decomposition of Indole Revisited. *ACS Phys. Chem. Au* **2022**, *2*, 225−236.
(37) Alessandrini, S.; Barone, V.; Puzzarini, C. Extension of the "Cheap" Composite Approach to Noncovalent Interactions: The jun-ChS Scheme. *J. Chem. Theory. Comput.* **2020**, *16*, 988−1006.
(38) Raghavachari, K.; Trucks, G. W.; Pople, J. A.; Head-Gordon, M. A fifth-order perturbation comparison of electron correlation theories. *Chem. Phys. Lett.* **1989**, *157*, 479−483.
(39) Puzzarini, C.; Barone, V. Extending the Molecular Size in Accurate Quantum-Chemical Calculations: The Equilibrium Structure and Spectroscopic Properties of Uracil. *Phys. Chem. Chem. Phys.* **2011**, *13*, 7189−7197.
(40) Puzzarini, C.; Biczysko, M.; Barone, V.; Largo, L.; Peña, I.; Cabezas, C.; Alonso, J. L. Accurate Characterization of the Peptide Linkage in the Gas Phase: A Joint Quantum-Chemical and Rotational Spectroscopy Study of the Glycine Dipeptide Analogue. *J. Phys. Chem. Lett.* **2014**, *5*, 534−540.
(41) Barone, V.; Lupi, J.; Salta, Z.; Tasinato, N. Development and validation of a parameter-free model chemistry for the computation of reliable reaction rates. *J. Chem. Theory Comput.* **2021**, *17*, 4913−4928.
(42) Møller, C.; Plesset, M. S. Note on an Approximation Treatment for Many-Electron Systems. *Phys. Rev.* **1934**, *46*, 618−622.
(43) Dunning, T. H. Gaussian basis sets for use in correlated molecular calculations. I. The atoms boron through neon and hydrogen. *J. Chem. Phys.* **1989**, *90*, 1007−1023.
(44) Woon, D. E.; Dunning, T. H. Gaussian basis sets for use in correlated molecular calculations. V. Core-valence basis sets for boron through neon. *J. Chem. Phys.* **1995**, *103*, 4572−4585.
(45) Peterson, K. A.; Dunning, T. H. Accurate correlation consistent basis sets for molecular core-valence correlation effects: The second row atoms Al-Ar, and the first row atoms B-Ne revisited. *J. Chem. Phys.* **2002**, *117*, 10548−10560.
(46) Werner, H.-J.; Adler, T. B.; Manby, F. R. General orbital invariant MP2-F12 theory. *J. Chem. Phys.* **2007**, *126*, 164102.
(47) Adler, T. B.; Knizia, G.; Werner, H.-J. A simple and efficient CCSD(T)-F12 approximation. *J. Chem. Phys.* **2007**, *127*, 221106.
(48) Lupi, J.; Alessandrini, S.; Barone, V.; Puzzarini, C. junChS and junChS-F12 Models: Parameter-free Efficient yet Accurate Composite Schemes for Energies and Structures of Noncovalent Complexes. *J. Chem. Theory Comput.* **2021**, *17*, 6974−6992.
(49) Barone, V.; et al. Bringing machine-learning enhanced quantum chemistry and microwave spectroscopy to conformational landscape exploration: the paradigmatic case of 4-fluoro-threonine. *Chemistry, Europ. J.* **2023**, *29*, No. e202203990.
(50) Barone, V.; Di Grande, S.; Puzzarini, C. Toward accurate yet effective computations of rotational spectroscopy parameters for biomolecule building blocks. *Molecules* **2023**, *28*, 913.
(51) Helgaker, T.; Klopper, W.; Koch, H.; Noga, J. Basis-set convergence of correlated calculations on water. *J. Chem. Phys.* **1997**, *106*, 9639−9646.
(52) Bloino, J.; Biczysko, M.; Barone, V. General Perturbative Approach for Spectroscopy, Thermodynamics, and Kinetics: Methodological Background and Benchmark Studies. *J. Chem. Theory Comput.* **2012**, *8*, 1015−1036.
(53) Frisch, M. J. et al. *Gaussian 16, Revision C.01*; Gaussian Inc.: 2016.
(54) Werner, H.-J.; Knowles, P. J.; Knizia, G.; Manby, F. R.; Schütz, M. Molpro: a general-purpose quantum chemistry program package. *WIREs Comput. Mol. Sci.* **2012**, *2*, 242−253.
(55) Werner, H.-J.; et al. The Molpro quantum chemistry package. *J. Chem. Phys.* **2020**, *152*, 144107.
(56) Werner, H.-J. et al. *MOLPRO*, version, a package of ab initio programs.
(57) Georgievskii, Y.; Miller, J. A.; Burke, M. P.; Klippenstein, S. J. Reformulation and Solution of the Master Equation for Multiple-Well Chemical Reactions. *J. Phys. Chem. A* **2013**, *117*, 12146−12154.
(58) Tardy, D. C.; Rabinovitch, B. S. Collisional Energy Transfer. Thermal Unimolecular Systems in the Low-Pressure Region. *J. Chem. Phys.* **1966**, *45*, 3720−3730.
(59) Pechukas, P.; Light, J. C. On Detailed Balancing and Statistical Theories of Chemical Kinetics. *J. Chem. Phys.* **1965**, *42*, 3281−3291.
(60) Chesnavich, W. J. Multiple transition states in unimolecular reactions. *J. Chem. Phys.* **1986**, *84*, 2615−2619.
(61) Fernández-Ramos, A.; Miller, J. A.; Klippenstein, S. J.; Truhlar, D. G. Modeling the Kinetics of Bimolecular Reactions. *Chem. Rev.* **2006**, *106*, 4518−4584.
(62) Eckart, C. The Penetration of a Potential Barrier by Electrons. *Phys. Rev.* **1930**, *35*, 1303−1309.
(63) Kooij, D. M. Über die Zersetzung des gasförmigen Phosphorwasserstoffs. *Zeitschr. Phys. Chem.* **1893**, *12U*, 155−161.
(64) Laidler, K. J. A glossary of terms used in chemical kinetics, including reaction dynamics (IUPAC Recommendations 1996). *Pure Appl. Chem.* **1996**, *68*, 149−192.
(65) Nandi, S.; Calderini, D.; Bloino, J.; Rampino, S.; Barone, V. A Modern-Fortran Program for Chemical Kinetics on Top of Anharmonic Vibrational Calculations. *Lect. Notes Comput. Sci.* **2019**, *11624*, 401−412.
(66) Nandi, S.; Ballotta, B.; Rampino, S.; Barone, V. A General User-Friendly Tool for Kinetic Calculations of Multi-Step Reactions within the Virtual Multifrequency Spectrometer Project. *Appl. Sci.* **2020**, *10*, 1872.
(67) Tishchenko, O.; Ilieva, S.; Truhlar, D. G. Communication: Energetics of reaction pathways for reactions of ethenol with the hydroxyl radical: The importance of internal hydrogen bonding at the transition state. *J. Chem. Phys.* **2010**, *133*, 021102.
(68) Guo, X.; Zhang, R. M.; Gao, L. G.; Zhang, X.; Xu, X. Computational kinetics of the hydrogen abstraction reactions of n-propanol and iso-propanol by OH radical. *Phys. Chem. Chem. Phys.* **2019**, *21*, 24458−24468.
(69) Zheng, J.; Oyedepo, G. A.; Truhlar, D. G. Kinetics of the Hydrogen Abstraction Reaction From 2-Butanol by OH Radical. *J. Phys. Chem. A* **2015**, *119*, 12182−12192.
(70) Gao, L. G.; Zheng, J.; Fernández-Ramos, A.; Truhlar, D. G.; Xu, X. Kinetics of the Methanol Reaction with OH at Interstellar, Atmospheric, and Combustion Temperatures. *J. Am. Chem. Soc.* **2018**, *140*, 2906−2918.

https://doi.org/10.1021/acsearthspacechem.3c00110
ACS Earth Space Chem. 2023, 7, 1467−1477